ACS Chemical Neuroscience

pubs.acs.org/chemneuro Research Article

Length and Unsaturation of Fatty Acids of Phosphatidic Acid Determines the Aggregation Rate of Insulin and Modifies the Structure and Toxicity of Insulin Aggregates

Mikhail Matveyenka,[‖] Stanislav Rizevsky,[‖] and Dmitry Kurouski*

Cite This: *ACS Chem. Neurosci.* 2022, 13, 2483−2489 Read Online

ACCESS | Metrics & More | Article Recommendations | Supporting Information

ABSTRACT: Phosphatidic acid (PA) is a unique plasma membrane lipid that contains fatty acids (FAs) with different lengths and degrees of unsaturation. Under physiological conditions, PA acts as a second messenger regulating a wide variety of cellular processes. At the same time, the role of PA under pathological conditions, which are caused by an abrupt aggregation of amyloid proteins, remains unclear. In this study, we investigated the effect of PA with different lengths and unsaturation of FAs on insulin aggregation. We found that PA with C16:0 FAs strongly inhibited insulin aggregation, whereas PA with C18:0 FAs accelerated it. Furthermore, PA with unsaturated (C18:1) FAs made the insulin form extremely long and thick fibrils that were not observed for PAs with saturated FAs. We also found that the presence of PA with C16:0 FAs resulted in the formation of aggregates that exerted significantly lower cell toxicity compared to the aggregates formed in the presence of PAs with C18:0 and C18:1 FAs. These results suggest that PA may play a key role in neurodegeneration.

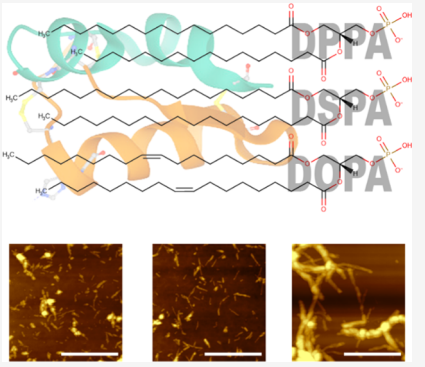

KEYWORDS: *aggregation rate, cell toxicity, neurodegeneration, plasma membrane*

INTRODUCTION

Phosphatidic acid (PA) is an anionic phospholipid that plays an important role in cell signaling and activation of lipid-gated ion channels.[1,2] PA contains both saturated and unsaturated fatty acids (FAs) at the *sn*-1 and *sn*-2 positions.[3] The degree of saturation of FAs and their length allows us to tailor the physiological activity of this phospholipid.[3] PA also constitutes around 0.25% of the plasma membrane, where it can uniquely alter membrane topology due to a cone-shaped geometry of the phospholipid.[4,5] These localized changes in membrane curvature determine membrane fusion and fission steps that are critical for vesicle trafficking.[6]

In addition to PA, plasma membranes contain phosphatidylcholine (PC), phosphatidylserine (PS), and other phospholipids.[5] A growing body of evidence suggests that both PC and PS can uniquely alter the aggregation properties of amyloid-associated proteins that include α-synuclein (α-Syn),[7] insulin[8,9] islet amyloid polypeptide protein,[10] and amyloid β peptide.[11] Abrupt aggregation of these proteins determines the onset and progression of amyloid diseases, including diabetes type 2 and Alzheimer's and Parkinson's diseases.[12,13] Galvagnion and co-workers demonstrated that lipids could lower the stability of α-Syn, facilitating its aggregation into fibrils, long twisted aggregates that had β-sheet secondary structure.[14−16] Our group found that lipids not only altered the rates of α-Syn aggregation but also uniquely modified the secondary structure of protein oligomers formed in their presence.[7] Recently, Rizevsky and co-workers showed that PC and cardiolipin (CL), a lipid that regulates electron transport complexes in mitochondria,[17,18] uniquely altered the stability of insulin, a small hormone that regulates glucose metabolism.[8,19] It has been found that CL drastically accelerated insulin aggregation, whereas PC strongly inhibited fibril formation. Furthermore, both PC and CL were found to be integrated into the structure of insulin oligomers and fibrils.[8,19] This drastically lowered toxicity of these protein aggregates compared to the insulin fibrils grown in the lipid-free environment.

Structural characterization of amyloid oligomers and fibrils is a challenging task. The transient nature of oligomers and their high structural heterogeneity limits the use of cryoelectron microscopy and solid-state nuclear magnetic resonance, classical tools of structural biology. A growing body of evidence suggests that atomic force microscopy infrared (AFM-IR) spectroscopy can be used to overcome these limitations.[20−24] In AFM-IR, a metallized scanning probe can be positioned directly at the sample of interest.[25] Next, the probe is illuminated by pulsed tunable IR light, which causes

Received: June 3, 2022
Accepted: July 26, 2022
Published: August 5, 2022

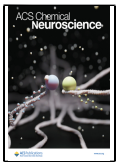

https://doi.org/10.1021/acschemneuro.2c00330
ACS Chem. Neurosci. 2022, 13, 2483−2489

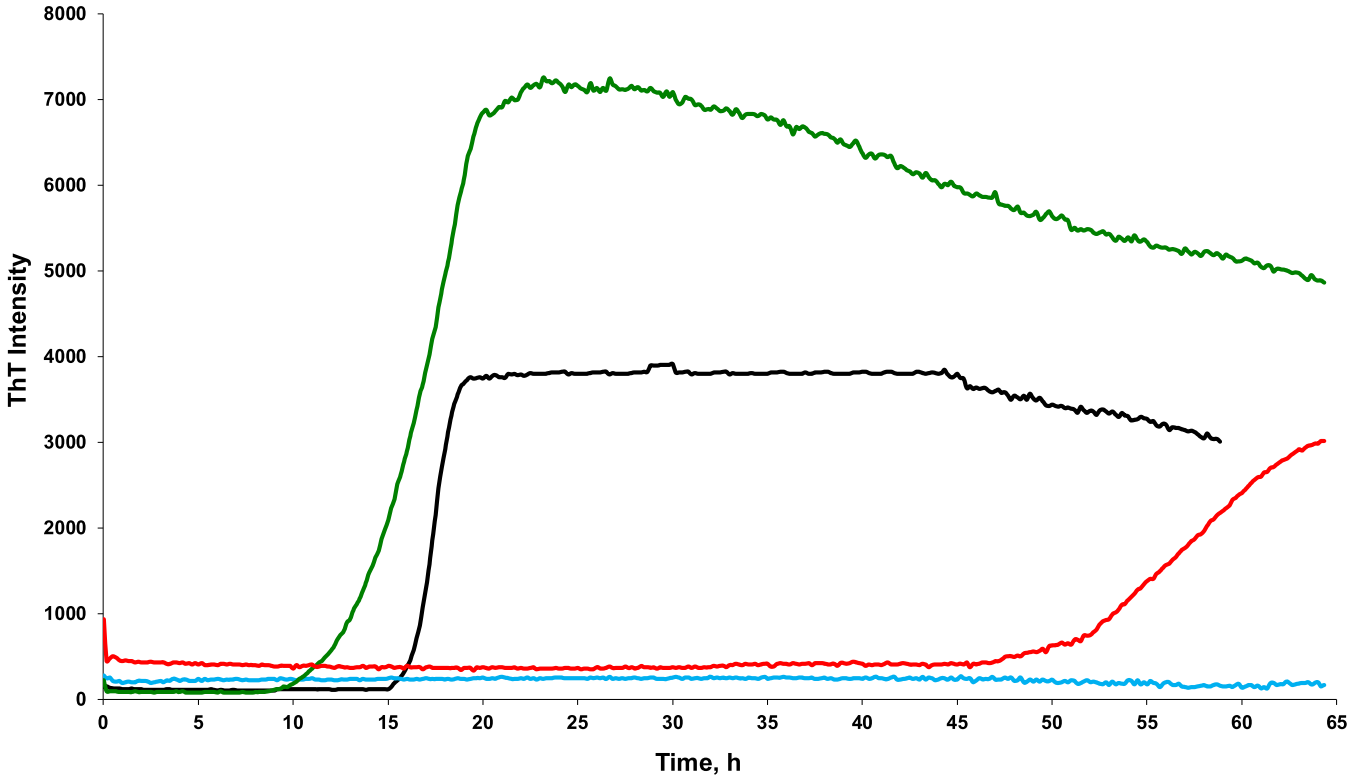

Figure 1. Saturation and lengths of FAs in PA uniquely alter the rate of insulin aggregation. ThT aggregation kinetics of insulin in the lipid-free environment (black) and in the presence of PA-$C_{18:0}$ (green), PA-$C_{18:1}$ (red), and PA-$C_{16:0}$ (light blue) at a 1:1 molar ratio.

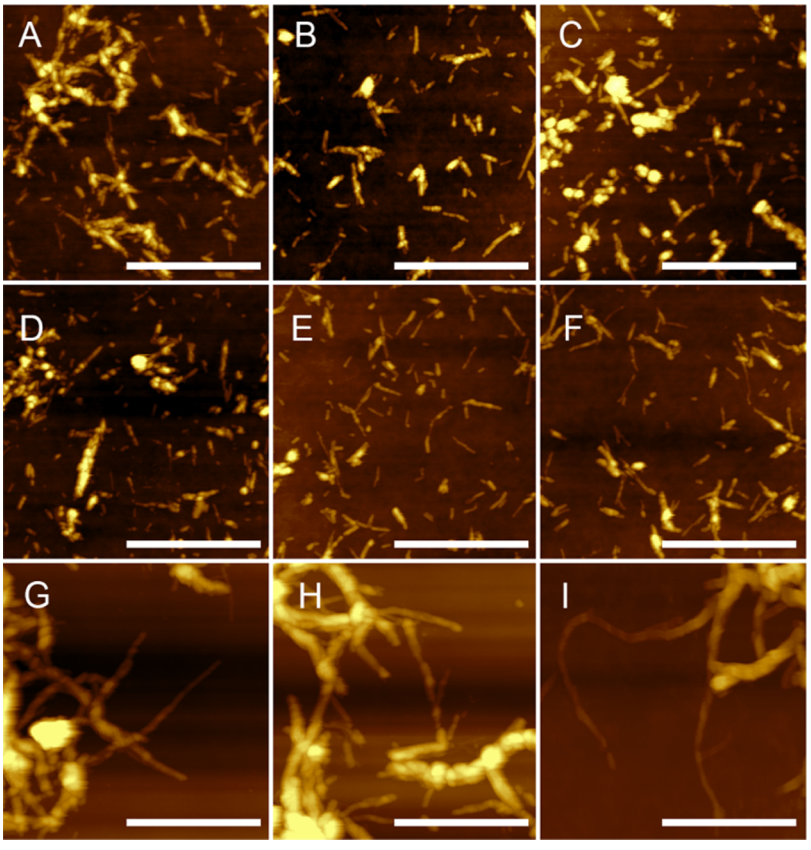

Figure 2. Saturation and lengths of FAs in PA uniquely alter morphologies of insulin aggregates. AFM images of insulin aggregates grown in the lipid-free environment (A, B), as well as in the presence of PA-$C_{16:0}$ (C, D), PA-$C_{18:0}$ (E, F), and PA-$C_{18:1}$ (G–I). Scale bars are 1 μm.

https://doi.org/10.1021/acschemneuro.2c00330
ACS Chem. Neurosci. 2022, 13, 2483−2489

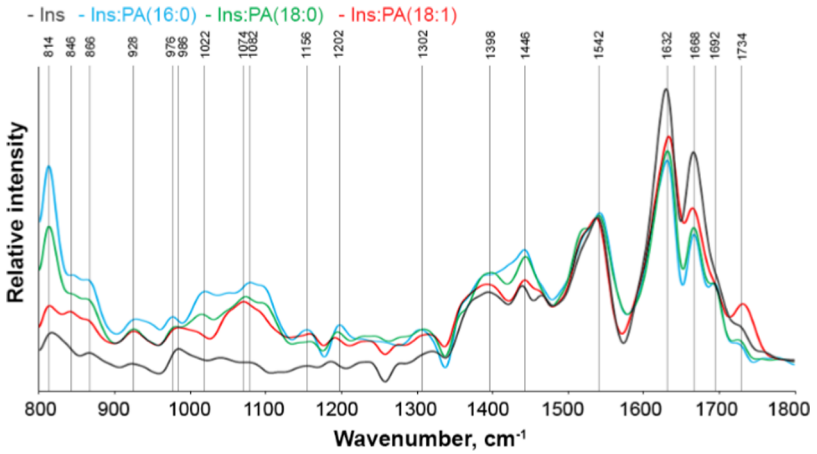

Figure 3. Nanoscale analysis of insulin (Ins), PA-$C_{16:0}$ (light blue), PA-$C_{18:0}$ (green), and PA-$C_{18:1}$ fibrils (red).

thermal expansions in the sample. These thermal expansions are reordered by the scanning probe and converted to the corresponding IR spectra.[26−28] Thus, AFM-IR allows us to acquire information about the secondary structure of individual oligomers and even individual proteins.[29,30] This high sensitivity and nanometer spatial resolution is utilized to reveal the secondary structure of amyloid fibrils,[20,22,23,31−33] plant epicuticular waxes,[34,35] polymers,[36] malaria-infected blood cells,[37] bacteria,[38−40] liposomes,[41] and polycrystalline perovskite films.[42]

In this study, we use a set of biophysical and molecular biology techniques to investigate the effect of PA on the aggregation properties of insulin. Insulin aggregation is observed for diabetes type 2 and injection amyloidosis.[43] Upon diabetes type 2, insulin overproduction in the pancreas causes protein misfolding and aggregation. Injection amyloidosis is characterized by high local concentrations of insulin created by hormone injection into the skin dermis.[44,45] This not only leads to insulin aggregation but can also catalyze aggregation of other proteins present in cell media, which may result in systemic amyloidosis.[46] We aggregate insulin in equimolar concentrations with PA that contains palmitic acids (saturated FAs with 16 carbons $C_{16:0}$), named hereafter PA-$C_{16:0}$, stearic acids (18 carbons $C_{18:0}$ FAs), named hereafter PA-$C_{18:0}$, as well as oleic acid (unsaturated FAs with one double bond $C_{18:1}$ FAs), named hereafter PA-$C_{18:1}$. Next, we used thioflavin T (ThT) assay to investigate the extent to which the length and saturation of FAs in PA alters the rate of insulin aggregation (Figure 1).

In the absence of lipids, insulin aggregation exhibits a well-defined lag phase (t_{lag} = 14.4 ± 0.8 h) that is characterized by the formation of oligomers (Figure 1). Once a critical concentration of these oligomers is reached, they rapidly propagate into fibrils. These protein aggregates bind ThT, which results in a strong interest in ThT fluorescence. We found that PA drastically alters t_{lag} of insulin aggregation. Specifically, PA-$C_{18:0}$ accelerates insulin aggregation (t_{lag} = 9.2 ± 0.1 h), whereas PA-$C_{18:1}$ drastically slows it down (t_{lag} = 46.3 ± 0.8 h). It should be noted that PA-$C_{16:0}$ fully inhibits insulin aggregation (Figure 1). Thus, saturation and lengths of FAs in PA play an important role in the modulation of insulin aggregation.

Nanoscale imaging of insulin aggregates grown in the lipid-free environment revealed the presence of fibrils with an average height of 12 nm (Figure 2). Aggregates with similar topologies were observed for PA-$C_{16:0}$ and PA-$C_{18:0}$. These fibrils had various lengths and heights ranging from 6 to 15 nm. However, PA-$C_{18:1}$ exhibited drastically different morphologies. These fibrils stretched for microns in length and had a much greater height that ranged from 15 to 30 nm. Thus, we could conclude that the presence of PA-$C_{16:0}$ and PA-$C_{18:0}$ did not significantly alter the topology of insulin aggregates, whereas the presence of PA-$C_{18:1}$ resulted in the formation of morphologically different fibrils that had drastically different dimensions compared to the insulin aggregates grown in the lipid-free environment.

Next, we utilize AFM-IR to examine the secondary structure of insulin aggregates grown in the presence of PA-$C_{16:0}$, PA-$C_{18:0}$, and PA-$C_{18:1}$, as well as insulin aggregates formed in the lipid-free environment (Ins) (Figure 3). The AFM-IR spectrum of Ins fibrils exhibits an amide II band around 1515−1542 cm^{-1} and an amide I band at 1630 and 1668 cm^{-1}. The position of the amide I band in the IR spectra of protein specimens can be used to determine their protein secondary structure. The amide I band around 1620−1635 cm^{-1} points on the predominance of a parallel β-sheet, whereas the localization of the amide I band around 1663 cm^{-1} band indicates the presence of an unordered protein in the secondary structure of the analyzed protein specimens. Based on this assignment, one can expect that insulin fibrils grown in the lipid-free environment are dominated by the parallel β-sheet with some unordered protein present in their secondary structure.[47,48]

In the AFM-IR spectra collected from PA-$C_{16:0}$ and PA-$C_{18:0}$, the amide I band was shifted to 1632 cm^{-1}, which indicated small changes in the conformation of the parallel β-sheet in these insulin aggregates. We also found that in the AFM-IR spectrum of PA-$C_{18:1}$, amide I was further red-shifted to 1634 cm^{-1}. This points to the structural differences between PA-$C_{18:1}$ fibrils and all other analyzed protein aggregates. We also observed differences in the peak area between ∼1634 and 1668 cm^{-1} bands in the AFM-IR spectra collected from PA-$C_{18:1}$, PA-$C_{16:0}$, and PA-$C_{18:0}$. Specifically, the ratio of the peak area of 1634 and 1668 cm^{-1} was ∼4:1 in the AFM-IR spectra collected from Ins, PA-$C_{16:0}$, and PA-$C_{18:0}$. However, in the spectrum collected from PA-$C_{18:1}$, the ratio of the peak area of 1634 and 1668 cm^{-1} was 9:1 (Figure S1). This spectroscopic evidence points to the very low content of unordered protein secondary structure in PA-$C_{18:1}$ compared to all other analyzed insulin aggregates.[47,49]

https://doi.org/10.1021/acschemneuro.2c00330
ACS Chem. Neurosci. 2022, 13, 2483−2489

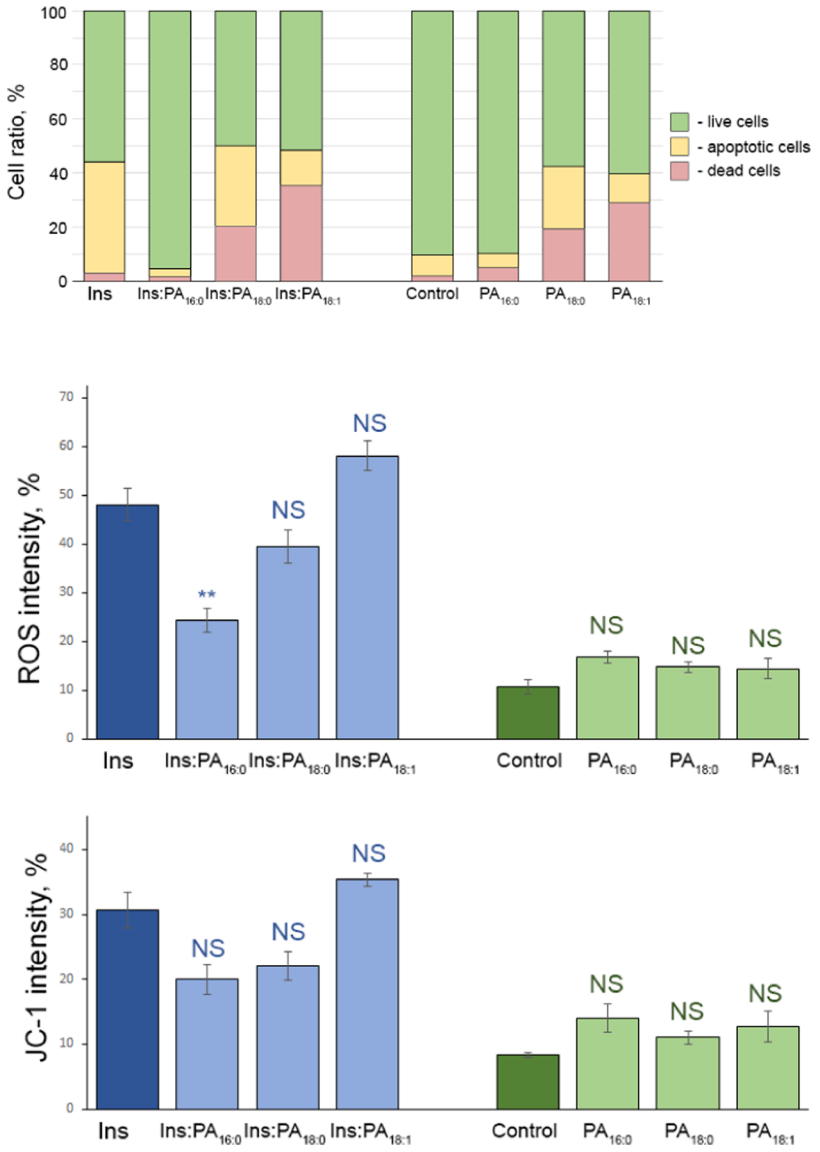

Figure 4. Annexin V cell viability assay, ROS, and mitochondrial stresses exerted by Ins, PA-$C_{16:0}$, PA-$C_{18:0}$, and PA-$C_{18:1}$. Histograms of cell viability (top) and ROS (middle) and JC-1 (bottom) assays of Ins, PA-$C_{16:0}$, PA-$C_{18:0}$, and PA-$C_{18:1}$ aggregates, as we as the corresponding PA-$C_{16:0}$, PA-$C_{18:0}$, and PA-$C_{18:1}$ lipids (green bars) themselves. Blue asterisks (*) and "NS" show the significance level of differences between Ins and insulin aggregates grown in the presence of lipids. Green "NS" shows the significance level of differences between the control and lipids themselves. NS: nonsignificant difference; $^{**}P \leq 0.01$.

We also found that the AFM-IR spectra collected from PA-$C_{18:1}$ exhibited an intense vibrational band around 1734 cm^{-1}, which could be assigned to the carbonyl vibration of the ester bonds of lipids. The same band was observed in the AFM-IR spectra collected from PA-$C_{16:0}$ and PA-$C_{18:0}$; however, with a significantly lower intensity. Based on this observation, we could conclude that lipids were present in the structures of PA-$C_{18:1}$, PA-$C_{16:0}$, and PA-$C_{18:0}$ aggregates. This conclusion was further supported by the observation of intense C−H (~800−866 cm^{-1}) and PO_2^- (976−1202 cm^{-1}) vibrations present in the AFM-IR spectra collected from PA-$C_{18:1}$, PA-$C_{16:0}$, and PA-$C_{18:0}$.[50] Presence of these bands, which were not evident in the AFM-IR spectrum of Ins, confirmed that the corresponding phospholipids were possessed by PA-$C_{18:1}$, PA-$C_{16:0}$, and PA-$C_{18:0}$ aggregates. We also observed differences in the spectroscopic profiles of C−H (~800 to 866 cm^{-1}) and PO_2^- (976−1202 cm^{-1}) bands in the AFM-IR spectra collected from PA-$C_{16:0}$, PA-$C_{18:0}$, and PA-$C_{18:1}$.[7,22,23,50] Specifically, C−H and PO_2^- vibrational bands and their intensities were very similar in the AFM-IR spectra collected from PA-$C_{16:0}$ and PA-$C_{18:0}$ aggregates. However, we observed a very low intensity of 1022 and 1446 cm^{-1} in the spectra collected from PA-$C_{18:1}$ fibrils, which was not evident in the AFM-IR spectra of PA-$C_{16:0}$ and PA-$C_{18:0}$. These findings suggested that ester groups of PA-$C_{18:1}$ had a different local environment in the structure of PA-C18:1 aggregates compared to the environment of PAs in the structure of PA-$C_{16:0}$ and PA-$C_{18:0}$ protein aggregates. Thus, there was a drastic difference between the interactions of saturated vs unsaturated PAs with insulin. This observation is in good agreement with the results reported by Mizuno and co-workers.[4]

The question to ask is whether observed structural differences between Ins, PA-$C_{16:0}$, PA-$C_{18:0}$, and PA-$C_{18:1}$ have any biological significance. To answer this question, we investigate the extent to which these protein aggregates exert

https://doi.org/10.1021/acschemneuro.2c00330
ACS Chem. Neurosci. 2022, 13, 2483−2489

cell toxicity, ROS, and mitochondrial stresses on the midbrain N27 cell line of the mice (Figure 4).

The cell viability assay showed that PA-$C_{16:0}$ exerted very little if any cell toxicity, whereas PA-$C_{18:0}$ and PA-$C_{18:1}$ fibrils were found to be toxic to N27 cells. It should be noted that cell toxicity of PA-$C_{18:0}$ and PA-$C_{18:1}$ fibrils was very similar to the toxicity exerted by Ins fibrils themselves. Our results also showed that PA-$C_{18:1}$ exerted more prompt toxicity effects, which resulted in a higher percentage of dead *vs* apoptotic cells, whereas the ratio between apoptotic and dead cells was different for Ins and PA-$C_{18:0}$. It should be noted that PA-$C_{16:0}$ lipid themselves were not toxic to cells. However, both PA-$C_{18:0}$ and PA-$C_{18:1}$ exerted significant cell toxicities.

Similar conclusions could be made about ROS levels exerted by insulin aggregates formed in the presence of PA-$C_{16:0}$. We found that these aggregates exert very low ROS levels in cells compared to Ins, PA-$C_{18:0}$, and PA-$C_{18:1}$. We also found that ROS levels exerted by PA-$C_{18:0}$ and PA-$C_{18:1}$ were not significantly different from the ROS levels exerted by Ins fibrils themselves. We also found that all analyzed aggregates cause similar stress on the mitochondrial activity of the cells. Finally, none of the lipids exerted significantly high ROS or mitochondrial impairment levels in the N27 cells.

DISCUSSION

Our results showed that the degree of unsaturation and the length of the FAs played an important role in the physiological activity of PA. Specifically, the presence of short FAs helped to stabilize insulin decelerating protein aggregation into fibrils. At the same time, an increase in the length of FAs on two carbon atoms had a tremendous effect on the behavior of PA. Instead of stabilization, PA-$C_{18:0}$ was found to strongly enhance the rate of insulin aggregation. It should be noted that morphologically similar aggregates were found in both PA-$C_{16:0}$ and PA-$C_{18:0}$. Thus, the length of the FAs had very little if any effect on the topology of insulin aggregates. At the same time, the presence of only one double bond drastically altered the behavior of PA. PA-$C_{18:1}$ both slowed down insulin aggregation and led to the formation of fibrils with drastically different morphologies compared to the aggregates formed in the presence of PA-$C_{18:0}$. One could expect that this effect could be explained by drastic differences between the interactions of PAs with saturated vs unsaturated FAs with insulin. Mizuno and co-workers recently reported that PA-$C_{18:1}$ was strongly bound to α-Syn, whereas the binding activity of PAs with saturated FAs was significantly lower.[4]

Our findings also show that the saturation of FAs in PA has a similar effect on the rate of insulin aggregation compared to the effect of saturation previously described by Matveyenka and co-workers for PS.[9] Specifically, saturated PS exhibit a much greater effect on the acceleration of insulin aggregation compared to the effect exerted by PS with one double bond present in its FAs. However, the effect of saturation of FAs of CL has an opposite effect on the rate of insulin aggregation. It has been shown that unsaturated CL much strongly accelerates insulin aggregation compared to its saturated analogue.[8] Nevertheless, the presence of unsaturated CL results in the formation of long fibrils that are not evident in the presence of saturated CL. These results point to the important role of hydrogen binding between the lipid and proteins. Such bonds are developed between the aliphatic FAs of lipids and hydrophobic amino acid residues. We infer that small differences in the hydrogen bonding between saturated and unsaturated FAs strongly influence the thermodynamics of the lipid:protein complex, which in turn, results in the structural and morphological differences discussed above. Differences in the thermodynamics of the lipid:protein complex can also explain the observed differences between PA-$C_{16:0}$ and PA-$C_{18:0}$. Two CH_2 groups drastically alter the melting points of such lipids and consistently should alter the thermodynamics of the lipid−protein interactions. Elucidation of the thermodynamic properties of PA-$C_{16:0}$−insulin, PA-$C_{18:0}$−insulin, and PA-$C_{18:1}$−insulin complexes is the subject of a separate study. Based on these results, we can conclude that the chemical nature of the phospholipid plays a critically important role in the stability of insulin and consequently its aggregation properties.

EXPERIMENTAL SECTION

Materials. Bovine insulin was purchased from Sigma-Aldrich (St. Louis, MO). 1,2-Dipalmitoyl-*sn*-glycero-3-phosphate (16:0/16:0-PA (PA-$C_{16:0}$)), 1,2-dioleoyl-*sn*-glycero-3-phosphate (18:1/18:1-PA (PA-$C_{16:1}$)), and 1,2-distealoyl-*sn*-3-phosphate (18:0/18:0-PA (PA-$C_{18:0}$)) were purchased from Avanti (Alabaster, AL).

Liposome Preparation. Large unilamellar vesicles (LUVs) of PA-$C_{16:0}$, PA-$C_{18:0}$, and PA-$C_{18:1}$ were prepared according to the method proposed by Galvagnion et al.[51] Briefly, 0.6 mg of each PA was dissolved in 2.6 mL of phosphate-buffered saline (PBS) with pH 7.4. After the lipid powder was fully dissolved, the solution was heated in a water bath to ∼50 °C for 30 min. Next, the solution was immersed in liquid nitrogen for 3−5 min. The procedure was repeated 8−10 times. After that, the lipid solution was subjected to fine reshaping on the LUVs using an extruder equipped with a 100 nm membrane (Avanti, Alabaster, AL). Dynamic light scattering was used to ensure that the size of the LUVs was within 100 ± 10 nm.

Insulin Aggregation. In the lipid-free environment, 400 μM insulin was dissolved in PBS. The solution pH was adjusted to 3.0 using concentrated HCl. For PA-$C_{16:0}$, PA-$C_{18:0}$, and PA-$C_{18:1}$, 400 μM insulin was mixed with an equivalent concentration of the corresponding lipid. The pH of the final solution was adjusted to 3.0 using concentrated HCl. Next, the samples were placed in a 96-well plate that was kept in a plate reader (Tecan, Männedorf, Switzerland) at 37 °C for 70 h under 510 rpm agitation.

Kinetic Measurements. Rates of protein aggregation were measured using a thioflavin T (ThT) fluorescence assay. For this, the samples were mixed with 2 mM ThT solution and placed in a 96-well plate that was kept in a plate reader (Tecan, Männedorf, Switzerland) at 37 °C for 70 h under 510 rpm agitation. Fluorescence measurements were taken every 10 min (excitation 450 nm; emission 488 nm).

AFM Imaging. Microscopic analysis of protein aggregates was performed on an AIST-NT-HORIBA system (Edison, NJ) using silicon AFM probes (force constant 2.7 N/m; resonance frequency 50−80 kHz) purchased from Appnano (Mountain View, CA). Preprocessing of the collected AFM images was made using AIST-NT software (Edison, NJ).

AFM-IR. AFM-IR spectra were collected on a Nano-IR3 system (Bruker, Santa Barbara, CA) equipped with a QCL laser using contact-mode AFM scanning probes (ContGB-G AFM probe, NanoAndMore, Watsonville, CA). The collected spectra were preprocessed using Bruker Imaging software.

Cell Toxicity Assays. Mice midbrain N27 cells were grown in RPMI 1640 Medium (Thermo Fisher Scientific, Waltham, MA) with 10% fetal bovine serum (FBS) (Invitrogen, Waltham, MA) in a 96-well plate (5000 cells per well) at 37 °C under 5% CO_2. After 24 h, the cells were found to fully adhere to the wells, reaching ∼70% confluency. Next, 100 μL of the cell culture was replaced with 100 μL of RPMI 1640 Medium with 5% FBS containing protein samples. After 24 h of incubation with the sample of the protein aggregates, the cells were stained using annexin V cell viability assay and analyzed on

https://doi.org/10.1021/acschemneuro.2c00330
ACS Chem. Neurosci. 2022, 13, 2483−2489

an LSRII BD flow cytometer (BD, San Jose, CA). All measurements were made in triplicates.

In parallel, reactive oxygen species (ROS) assay was performed using the same cell culture. Briefly, ROS reagent (C10422, Invitrogen, Waltham, MA) was added to reach the final concentration of 5 μM and incubated at 37 °C under 5% CO_2 for 30 min. After the supernatant was removed, the cells were washed with PBS and resuspended in 200 μL of PBS in the flow cytometry tubes. Sample measurements were made in an LSRII BD flow cytometer (BD, San Jose, CA) using a red channel (λ = 633 nm). Percentages of ROS cells were determined using LSRII software. A *t*-test was used to determine the significance level of differences between the toxicity of the analyzed samples.

For JC-1 staining, 1 μL of a JC-1 reagent (M34152A, Invitrogen, Waltham, MA) was added to the cells and incubated at 37 °C under 5% CO_2 for 30 min. After the supernatant was removed, the cells were washed with PBS and resuspended in 200 μL of PBS in the flow cytometry tubes. Sample measurements were made in an LSRII BD flow cytometer (BD, San Jose, CA) using a red channel (λ = 633 nm). Percentages of ROS cells were determined using LSRII BD software. A *t*-test was used to determine the significance level of differences between the toxicity of the analyzed samples.

■ ASSOCIATED CONTENT

Supporting Information

The Supporting Information is available free of charge at https://pubs.acs.org/doi/10.1021/acschemneuro.2c00330.

Figure S1 shows a histogram of amide I % areas of parallel β-sheet and unordered protein in the AFM-IR spectra reported in Figure 3 (PDF)

■ AUTHOR INFORMATION

Corresponding Author

Dmitry Kurouski − *Department of Biochemistry and Biophysics, Texas A&M University, College Station, Texas 77843, United States; Department of Biomedical Engineering, Texas A&M University, College Station, Texas 77843, United States;* orcid.org/0000-0002-6040-4213; Phone: 979-458-3778; Email: dkurouski@tamu.edu

Authors

Mikhail Matveyenka − *Department of Biochemistry and Biophysics, Texas A&M University, College Station, Texas 77843, United States*

Stanislav Rizevsky − *Department of Biochemistry and Biophysics, Texas A&M University, College Station, Texas 77843, United States; Department of Biotechnology, Binh Duong University, Thu Dau Mot 820000, Vietnam*

Complete contact information is available at: https://pubs.acs.org/10.1021/acschemneuro.2c00330

Author Contributions

‖M.M. and S.R. contributed equally.

Notes

The authors declare no competing financial interest.

■ ACKNOWLEDGMENTS

The authors are grateful to the National Institute of Health for the provided financial support (R35GM142869).

■ REFERENCES

(1) Tanguy, E.; Wang, Q. L.; Moine, H.; Vitale, N. Phosphatidic Acid: From Pleiotropic Functions to Neuronal Pathology. *Front. Cell. Neurosci.* **2019**, *13*, No. 2.

(2) Bader, M. F.; Vitale, N. Phospholipase D in Calcium-Regulated Exocytosis: Lessons from Chromaffin Cells. *Biochim. Biophys. Acta* **2009**, *1791*, 936−941.

(3) Stace, C. L.; Ktistakis, N. T. Phosphatidic Acid- and Phosphatidylserine-Binding Proteins. *Biochim. Biophys. Acta* **2006**, *1761*, 913−926.

(4) Mizuno, S.; Sasai, H.; Kume, A.; Takahashi, D.; Satoh, M.; Kado, S.; Sakane, F. Dioleoyl-Phosphatidic Acid Selectively Binds to Alpha-Synuclein and Strongly Induces Its Aggregation. *FEBS Lett.* **2017**, *591*, 784−791.

(5) Fitzner, D.; Bader, J. M.; Penkert, H.; Bergner, C. G.; Su, M.; Weil, M. T.; Surma, M. A.; Mann, M.; Klose, C.; Simons, M. Cell-Type- and Brain-Region-Resolved Mouse Brain Lipidome. *Cell Rep.* **2020**, *32*, No. 108132.

(6) McMahon, H. T.; Gallop, J. L. Membrane Curvature and Mechanisms of Dynamic Cell Membrane Remodelling. *Nature* **2005**, *438*, 590−596.

(7) Dou, T.; Zhou, L.; Kurouski, D. Unravelling the Structural Organization of Individual Alpha-Synuclein Oligomers Grown in the Presence of Phospholipids. *J. Phys. Chem. Lett.* **2021**, *12*, 4407−4414.

(8) Matveyenka, M.; Rizevsky, S.; Kurouski, D. Unsaturation in the Fatty Acids of Phospholipids Drastically Alters the Structure and Toxicity of Insulin Aggregates Grown in Their Presence. *J. Phys. Chem. Lett.* **2022**, *13*, 4563−4569.

(9) Matveyenka, M.; Rizevsky, S.; Kurouski, D. The Degree of Unsaturation of Fatty Acids in Phosphatidylserine Alters the Rate of Insulin Aggregation and the Structure and Toxicity of Amyloid Aggregates. *FEBS Lett.* **2022**, *596*, 1424−1433.

(10) Zhang, X.; St Clair, J. R.; London, E.; Raleigh, D. P. Islet Amyloid Polypeptide Membrane Interactions: Effects of Membrane Composition. *Biochemistry* **2017**, *56*, 376−390.

(11) Avdulov, N. A.; Chochina, S. V.; Igbavboa, U.; Warden, C. S.; Vassiliev, A. V.; Wood, W. G. Lipid Binding to Amyloid Beta-Peptide Aggregates: Preferential Binding of Cholesterol as Compared with Phosphatidylcholine and Fatty Acids. *J. Neurochem.* **1997**, *69*, 1746−1752.

(12) Chiti, F.; Dobson, C. M. Protein Misfolding, Amyloid Formation, and Human Disease: A Summary of Progress over the Last Decade. *Annu. Rev. Biochem.* **2017**, *86*, 27−68.

(13) Knowles, T. P. J.; Vendruscolo, M.; Dobson, C. M. The Amyloid State and Its Association with Protein Misfolding Diseases. *Nat. Rev. Mol. Cell Biol.* **2014**, *15*, 384−396.

(14) Alza, N. P.; Iglesias Gonzalez, P. A.; Conde, M. A.; Uranga, R. M.; Salvador, G. A. Lipids at the Crossroad of Alpha-Synuclein Function and Dysfunction: Biological and Pathological Implications. *Front. Cell. Neurosci.* **2019**, *13*, 175.

(15) Galvagnion, C. The Role of Lipids Interacting with -Synuclein in the Pathogenesis of Parkinson's Disease. *J. Parkinson Dis.* **2017**, *7*, 433−450.

(16) Galvagnion, C.; Brown, J. W.; Ouberai, M. M.; Flagmeier, P.; Vendruscolo, M.; Buell, A. K.; Sparr, E.; Dobson, C. M. Chemical Properties of Lipids Strongly Affect the Kinetics of the Membrane-Induced Aggregation of Alpha-Synuclein. *Proc. Natl. Acad. Sci. U.S.A.* **2016**, *113*, 7065−7070.

(17) Pope, S.; Land, J. M.; Heales, S. J. Oxidative Stress and Mitochondrial Dysfunction in Neurodegeneration; Cardiolipin a Critical Target? *Biochim. Biophys. Acta* **2008**, *1777*, 794−799.

(18) Falabella, M.; Vernon, H. J.; Hanna, M. G.; Claypool, S. M.; Pitceathly, R. D. S. Cardiolipin, Mitochondria, and Neurological Disease. *Trends Endocrinol. Metab.* **2021**, *32*, 224−237.

(19) Rizevsky, S.; Matveyenka, M.; Kurouski, D. Nanoscale Structural Analysis of a Lipid-Driven Aggregation of Insulin. *J. Phys. Chem. Lett.* **2022**, *13*, 2467−2473.

(20) Rizevsky, S.; Kurouski, D. Nanoscale Structural Organization of Insulin Fibril Polymorphs Revealed by Atomic Force Microscopy-Infrared Spectroscopy (Afm-Ir). *ChemBioChem* **2020**, *21*, 481−485.

(21) Ruggeri, F. S.; Charmet, J.; Kartanas, T.; Peter, Q.; Chia, S.; Habchi, J.; Dobson, C. M.; Vendruscolo, M.; Knowles, T. P. J.

Microfluidic Deposition for Resolving Single-Molecule Protein Architecture and Heterogeneity. *Nat. Commun.* **2018**, *9*, No. 3890.
(22) Ruggeri, F. S.; Flagmeier, P.; Kumita, J. R.; Meisl, G.; Chirgadze, D. Y.; Bongiovanni, M. N.; Knowles, T. P. J.; Dobson, C. M. The Influence of Pathogenic Mutations in Alpha-Synuclein on Biophysical and Structural Characteristics of Amyloid Fibrils. *ACS Nano* **2020**, *14*, 5213−5222.
(23) Ruggeri, F. S.; Longo, G.; Faggiano, S.; Lipiec, E.; Pastore, A.; Dietler, G. Infrared Nanospectroscopy Characterization of Oligomeric and Fibrillar Aggregates During Amyloid Formation. *Nat. Commun.* **2015**, *6*, No. 7831.
(24) Zhou, L.; Kurouski, D. Structural Characterization of Individual Alpha-Synuclein Oligomers Formed at Different Stages of Protein Aggregation by Atomic Force Microscopy-Infrared Spectroscopy. *Anal. Chem.* **2020**, *92*, 6806−6810.
(25) Rizevsky, S.; Zhaliazka, M.; Dou, T.; Matveyenka, M. Characterization of Substrates and Surface-Enhancement in Atomic Force Microscopy Infrared (Afm-Ir) Analysis of Amyloid Aggregates. *J. Phys. Chem. C* **2022**, *126*, 4157−4162.
(26) Dazzi, A.; Glotin, F.; Carminati, R. Theory of Infrared Nanospectroscopy by Photothermal Induced Resonance. *J. Appl. Phys.* **2010**, *107*, No. 124519.
(27) Dazzi, A.; Prater, C. B. Afm-Ir: Technology and Applications in Nanoscale Infrared Spectroscopy and Chemical Imaging. *Chem. Rev.* **2017**, *117*, 5146−5173.
(28) Kurouski, D.; Dazzi, A.; Zenobi, R.; Centrone, A. Infrared and Raman Chemical Imaging and Spectroscopy at the Nanoscale. *Chem. Soc. Rev.* **2020**, *49*, 3315−3347.
(29) Ruggeri, F. S.; Mannini, B.; Schmid, R.; Vendruscolo, M.; Knowles, T. P. J. Single Molecule Secondary Structure Determination of Proteins through Infrared Absorption Nanospectroscopy. *Nat. Commun.* **2020**, *11*, No. 2945.
(30) Lu, F.; Jin, M. Z.; Belkin, M. A. Tip-Enhanced Infrared Nanospectroscopy Via Molecular Expansion Force Detection. *Nat. Photonics* **2014**, *8*, 307−312.
(31) Ruggeri, F. S.; Benedetti, F.; Knowles, T. P. J.; Lashuel, H. A.; Sekatskii, S.; Dietler, G. Identification and Nanomechanical Characterization of the Fundamental Single-Strand Protofilaments of Amyloid Alpha-Synuclein Fibrils. *Proc. Natl. Acad. Sci. U.S.A.* **2018**, *115*, 7230−7235.
(32) Ruggeri, F. S.; Vieweg, S.; Cendrowska, U.; Longo, G.; Chiki, A.; Lashuel, H. A.; Dietler, G. Nanoscale Studies Link Amyloid Maturity with Polyglutamine Diseases Onset. *Sci. Rep.* **2016**, *6*, No. 31155.
(33) Ramer, G.; Ruggeri, F. S.; Levin, A.; Knowles, T. P. J.; Centrone, A. Determination of Polypeptide Conformation with Nanoscale Resolution in Water. *ACS Nano* **2018**, *12*, 6612−6619.
(34) Farber, C.; Li, J.; Hager, E.; Chemelewski, R.; Mullet, J.; Rogachev, A. Y.; Kurouski, D. Complementarity of Raman and Infrared Spectroscopy for Structural Characterization of Plant Epicuticular Waxes. *ACS Omega* **2019**, *4*, 3700−3707.
(35) Farber, C.; Wang, R.; Chemelewski, R.; Mullet, J.; Kurouski, D. Nanoscale Structural Organization of Plant Epicuticular Wax Probed by Atomic Force Microscope Infrared Spectroscopy. *Anal. Chem.* **2019**, *91*, 2472−2479.
(36) Dazzi, A. Photothermal Induced Resonance. Application to Infrared Spectromicroscopy. In *Thermal Nanosystems and Nanomaterials* Volz, S., Ed.; Springer: Berlin, 2009; Vol. *118*, pp 469−503.
(37) Perez-Guaita, D.; Kochan, K.; Batty, M.; Doerig, C.; Garcia-Bustos, J.; Espinoza, S.; McNaughton, D.; Heraud, P.; Wood, B. R. Multispectral Atomic Force Microscopy-Infrared Nano-Imaging of Malaria Infected Red Blood Cells. *Anal. Chem.* **2018**, *90*, 3140−3148.
(38) Dazzi, A.; Prazeres, R.; Glotin, F.; Ortega, J. M.; Al-Sawaftah, M.; de Frutos, M. Chemical Mapping of the Distribution of Viruses into Infected Bacteria with a Photothermal Method. *Ultramicroscopy* **2008**, *108*, 635−641.
(39) Mayet, C.; Deniset-Besseau, A.; Prazeres, R.; Ortega, J. M.; Dazzi, A. Analysis of Bacterial Polyhydroxybutyrate Production by Multimodal Nanoimaging. *Biotechnol. Adv.* **2013**, *31*, 369−374.
(40) Kochan, K.; Perez-Guaita, D.; Pissang, J.; Jiang, J. H.; Peleg, A. Y.; McNaughton, D.; Heraud, P.; Wood, B. R. In Vivo Atomic Force Microscopy-Infrared Spectroscopy of Bacteria. *J. R. Soc. Interface* **2018**, *15*, No. 20180115.
(41) Wieland, K.; Ramer, G.; Weiss, V. U.; Allmaier, G.; Lendl, B.; Centrone, A. Nanoscale Chemical Imaging of Individual Chemotherapeutic Cytarabine-Loaded Liposomal Nanocarriers. *Nano Res.* **2019**, *12*, 197−203.
(42) Strelcov, E.; Dong, Q.; Li, T.; Chae, J.; Shao, Y.; Deng, Y.; Gruverman, A.; Huang, J.; Centrone, A. Ch3nh3pbi3 Perovskites: Ferroelasticity Revealed. *Sci. Adv.* **2017**, *3*, No. e1602165.
(43) D'Souza, A.; Theis, J. D.; Vrana, J. A.; Buadi, F.; Dispenzieri, A.; Dogan, A. Localized Insulin-Derived Amyloidosis: A Potential Pitfall in the Diagnosis of Systemic Amyloidosis by Fat Aspirate. *Am. J. Hematol.* **2012**, *87*, E131−E132.
(44) Gupta, Y.; Singla, G.; Singla, R. Insulin-Derived Amyloidosis. *Indian J. Endocrinol. Metab.* **2015**, *19*, 174−177.
(45) Shikama, Y.; Kitazawa, J.; Yagihashi, N.; Uehara, O.; Murata, Y.; Yajima, N.; Wada, R.; Yagihashi, S. Localized Amyloidosis at the Site of Repeated Insulin Injection in a Diabetic Patient. *Intern. Med.* **2010**, *49*, 397−401.
(46) Iwaya, K.; Zako, T.; Fukunaga, J.; et al. Toxicity of Insulin-Derived Amyloidosis: A Case Report. *BMC Endocrine Disord.* **2019**, *19*, 61.
(47) Kurouski, D.; Lombardi, R. A.; Dukor, R. K.; Lednev, I. K.; Nafie, L. A. Direct Observation and Ph Control of Reversed Supramolecular Chirality in Insulin Fibrils by Vibrational Circular Dichroism. *Chem. Commun.* **2010**, *46*, 7154−7156.
(48) Sarroukh, R.; Goormaghtigh, E.; Ruysschaert, J. M.; Raussens, V. Atr-Ftir: A "Rejuvenated" Tool to Investigate Amyloid Proteins. *Biochim. Biophys. Acta* **2013**, *1828*, 2328−2338.
(49) Barth, A. Infrared Spectroscopy of Proteins. *Biochim. Biophys. Acta* **2007**, *1767*, 1073−1101.
(50) Dou, T.; Li, Z.; Zhang, J.; Evilevitch, A.; Kurouski, D. Nanoscale Structural Characterization of Individual Viral Particles Using Atomic Force Microscopy Infrared Spectroscopy (Afm-Ir) and Tip-Enhanced Raman Spectroscopy (Ters). *Anal. Chem.* **2020**, *92*, 11297−11304.
(51) Galvagnion, C.; Buell, A. K.; Meisl, G.; Michaels, T. C. T.; Vendruscolo, M.; Knowles, T. P. J.; Dobson, C. M. Lipid Vesicles Trigger A-Synuclein Aggregation by Stimulating Primary Nucleation. *Nat. Chem. Biol.* **2015**, *11*, 229−234.

https://doi.org/10.1021/acschemneuro.2c00330
ACS Chem. Neurosci. 2022, 13, 2483−2489